npj | quantum materials

Article

Published in partnership with Nanjing University

https://doi.org/10.1038/s41535-025-00757-4

Spin-orbit-entangled state of Ba_2CaOsO_6 studied by O *K*-edge resonant inelastic X-ray scattering and Raman spectroscopy

J. Okamoto[1], G. Shibata[2], Yu. S. Ponosov[3], H. Hayashi[4,5,11], K. Yamaura[4,5], H. Y. Huang[1], A. Singh[1], C. T. Chen[1], A. Tanaka[6], S. V. Streltsov[3] ✉, D. J. Huang[1,7,8] ✉ & A. Fujimori[1,2,9,10] ✉

Transition-metal ions with $5d^2$ electronic configuration in a cubic crystal field are prone to have a vanishing dipolar magnetic moment but finite higher-order multipolar moments, and they are expected to exhibit exotic physical properties. Through an investigation using resonant inelastic X-ray scattering (RIXS), Raman spectroscopy, and theoretical ligand-field (LF) multiplet and ab initio calculations, we fully characterized the local electronic structure of Ba_2CaOsO_6, particularly, the crystal-field symmetry of the $5d^2$ electrons in this anomalous material. The low-energy multiplet excitations from RIXS at the oxygen *K* edge and Raman-active phonons both show no splitting. These findings are consistent with the ground state of Os ions dominated by magnetic octupoles. Obtained parameters pave the way for further realistic microscopic studies of this highly unusual class of materials, advancing our understanding of spin-orbit physics in systems with higher-order multipoles.

$5d$ transition-metal oxides exhibit various exotic physical properties arising from the strong spin-orbit coupling (SOC) that competes with Hund's coupling and Jahn-Teller effect and strongly influences the exchange interaction[1–3]. Particularly attractive have been the Mott-insulating Ir^{4+} ($5d^5$) compounds with effective angular momentum $J_{\rm eff} = 1/2$ and the Kitaev quantum-spin-liquid candidate of Ru^{3+} ($4d^5$) honeycomb lattices. Especially exotic are localized $5d^2$ electrons in a cubic crystal field. A d^2 ion coordinated by ligand atoms in the octahedral (O_h) environment is expected to be Jahn-Teller active, but many cubic crystals with $5d^2$ ions remain undistorted, probably due to the strong SOC of the $5d$ electrons[4]. Such a $5d^2$ ion in the O_h-symmetry crystal field has a non-Kramers doublet ground state that supports either an electric quadrupole or a magnetic octupole[5–9]. This is contrasted with $5d^1$ systems, where the $5d$ ion has an electric quadrupole and Jahn-Teller distortion is induced[1,2,4,7,10]. As a staggered octupolar order has been predicted theoretically for quarter-filled manganites[11], one may conceive disordered octupoles or a quantum octupole liquid under particular conditions in manganites or other materials.

The *B*-site-ordered double perovskite Ba_2AOsO_6, where *A* is an alkali-earth metal, is one of such $5d^2$ (Os^{6+}) systems. The face-centered cubic (fcc) lattice formed by the Os ions may induce geometrical frustrations between the multipoles, and may lead to intriguing quantum magnetism predicted theoretically[5–9]. For example, Ba_2CaOsO_6 shows a cusp-like anomaly in the magnetic susceptibility at $T^* \sim 50$ K, signaling a magnetic transition, and muon-spin rotation (μ-SR) has revealed a small magnetic moment of ~0.2 μ_B[12] or ~0.05 μ_B per Os ion[13] whereas neutron scattering has detected no magnetic Bragg peaks below T^*[12]. (According to ref. 13, the small magnetic moment may be induced by impurities and may not be intrinsic.) According to X-ray diffraction, the crystal remains cubic down to the lowest temperatures[14]. This precludes static electric quadrupolar order, which should distort the cubic lattice[10], but is consistent with magnetic octupolar order as the origin of the 'hidden order' in Ba_2AOsO_6. Theoretically, exchange coupling between neighboring Os ions favors ferro-octupolar order in the fcc lattice[6].

In an O_h-symmetry crystal field, the one-electron Os $5d$ level is split into the t_{2g} and e_g levels separated by $\Delta_{\rm LF}$ [Fig. 1a]. The strong SOC splits the

[1]National Synchrotron Radiation Research Center, Hsinchu, 300092, Taiwan. [2]Materials Sciences Research Center, Japan Atomic Energy Agency, Sayo, Hyogo, 679-5148, Japan. [3]Institute of Metal Physics, Yekaterinburg, 620041 GSP-170, Russia. [4]Research Center for Materials Nanoarchitectonics (MANA), National Institute for Materials Science, Tsukuba, Ibaraki, 305-0044, Japan. [5]Graduate School of Chemical Sciences and Engineering, Hokkaido University, Sapporo, Hokkaido, 060-0810, Japan. [6]Graduate School of Advanced Science and Engineering, Hiroshima University, Higashi-Hiroshima, 739-8530, Japan. [7]Department of Physics, National Tsing Hua University, Hsinchu, 300044, Taiwan. [8]Department of Electrophysics, National Yang Ming Chiao Tung University, Hsinchu, 300093, Taiwan. [9]Center for Quantum Science and Technology and Department of Physics, National Tsing Hua University, Hsinchu, 300044, Taiwan. [10]Department of Physics, The University of Tokyo, Bunkyo-Ku, Tokyo, 113-0033, Japan. [11]Present address: Institute for Solid State Physics, The University of Tokyo, 5-1-5 Kashiwanoha, Kashiwa, Chiba, 277-8581, Japan. ✉e-mail: streltsov@imp.uran.ru; djhuang@nsrrc.org.tw; fujimori@phys.s.u-tokyo.ac.jp

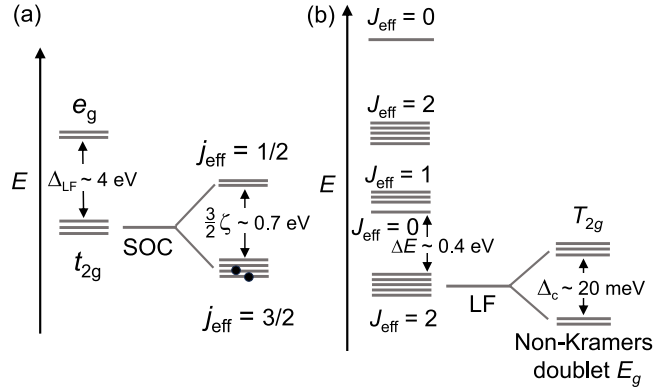

Fig. 1 | Energy diagrams of the Os^{6+} ($5d^2$) ion in the cubic (O_h) crystal field. a One-electron energy diagram. Δ_{LF} is the t_{2g}-e_g splitting. Spin-orbit coupling (SOC) further splits the t_{2g} level into $j_{eff} = \frac{1}{2}$ and $j_{eff} = \frac{3}{2}$ levels separated by $\frac{3}{2}\zeta$, and the $j_{eff} = \frac{3}{2}$ level is occupied by two electrons. **b** Two-electron energy diagram. The t_{2g}^2 part of the d^2 multiplet is shown whereas the $t_{2g}e_g$ part is located at higher energies separated by ~ Δ_{LF}. Due to the ligand field (LF) of cubic symmetry, the $J_{eff} = 2$ ground state is split by a 'residual' cubic splitting Δ_c into the non-Kramers E_g doublet and the T_{2g} triplet. The first $J_{eff} = 0$ excited state appears ΔE ~ 0.4 eV above the ground state, and the first $J_{eff} = 1$ excited state ~ 0.065 eV above it.

t_{2g} level into the $j_{eff} = \frac{1}{2}$ and $j_{eff} = \frac{3}{2}$ sublevels, and the latter is occupied by the two electrons of the Os^{6+} ion. In the two-electron energy diagram [Fig. 1b], the ground state has the total effective angular momentum of $J_{eff} = 2$. Under the O_h symmetry, the 'residual' cubic crystal-field splits the $J_{eff} = 2$ quintet into the ground-state E_g doublet and the triply-degenerate T_{2g} excited states with a separation Δ_c[14,15]. The E_g ground state is a non-Kramers doublet consisting of $|\psi_{g,\uparrow}\rangle \equiv |J^z_{eff} = 0\rangle$ and $|\psi_{g,\downarrow}\rangle \equiv \frac{1}{\sqrt{2}}(|J^z_{eff} = 2\rangle + |J^z_{eff} = -2\rangle)$, whereas the T_{2g} excited states consist of $|\psi_{e,\pm}\rangle \equiv |J^z_{eff} = \pm 1\rangle$ and $|\psi_{e,0}\rangle \equiv \frac{1}{\sqrt{2}}(|J^z_{eff} = 2\rangle - |J^z_{eff} = -2\rangle)$. In the ferro-octupole-ordered state, all the Os ions are in one of the two eigenstates, $|\psi_{g,\pm}\rangle \equiv \frac{1}{\sqrt{2}}(|\psi_{g,\uparrow}\rangle \pm i|\psi_{g,\downarrow}\rangle)$, of the octupole operator $T_{xyz} \propto \overline{J^x J^y J^z}$, where the overline denotes symmetrization.

While the magnetic properties of Ba_2AOsO_6 double perovskites have been widely studied and microscopic models to explain the observed anomalies have been proposed, their electronic structure remains unexplored experimentally. The present paper aims to fill this gap. In particular, we studied Ba_2CaOsO_6 by X-ray absorption spectroscopy (XAS) and resonant inelastic X-ray scattering (RIXS) at the O *K* edge. RIXS studies of 5*d* transition-metal oxides have so far been performed mainly at the transition-metal $L_{2,3}$ edge since one can directly study the spin and orbital excitation of the 5*d* states[16–19]. However, owing to the strong SOC of the 5*d* electrons, RIXS at the O *K* edge can also be used to study spin excitations [Fig. 1b][20–24]. O *K*-edge RIXS has the advantage of having higher energy resolution than transition-metal $L_{2,3}$-edge RIXS, allowing us to study low-energy electronic excitation and electron-phonon interaction. We have also utilized Raman scattering to detect possible local lattice distortion that induces low-symmetry crystal fields. None of the above measurements have indeed shown evidence for the lowering of the cubic symmetry, favoring the scenario that the Os ions have dominantly octupolar moments in Ba_2CaOsO_6.

Results and analyses

We performed O *K*-edge RIXS on high-quality polycrystalline samples with the energy resolution of ~30 meV using π polarized X-rays and 90° scattering angle (see Methods). The O *K*-edge XAS spectrum is shown in Fig. 2a. Figure 2b shows the RIXS intensity map in the E_{in}-E_{loss} plane, where E_{in} is the energy of incident X-ray and E_{loss} is the energy loss of scattered X-rays. The same data are plotted in the E_{in}-E_{em} plane in Fig. 2c, where E_{em} is the energy of emitted X-ray. RIXS spectra are plotted in Fig. 2d. In the figure, above E_{in} ~ 529 eV, some spectral features start to shift to higher E_{loss} with increasing E_{in}, indicating a cross-over from Raman-like to fluorescence-like.

Splitting due to ligand field and spin-orbit coupling

In O *K*-edge RIXS, the excitation of the O 1*s* core electron into empty states followed by the electron transition from the non-bonding O 2*p* band to the O 1*s* core level leaves a hole in the non-bonding O 2*p* band and an electron in the empty states. The resulting final state is equivalent to that of the O 2*p* → Os 5*d* charge-transfer (CT) excitation, which measures the unoccupied part of the O 2*p* partial density of states (PDOS). Because the energy position of the non-bonding O 2*p* band is located near the top of the O 2*p* band, we assumed it located ~ 2 eV below the Fermi level (E_F), based on the occupied O 2*p* PDOS deduced from fluorescence spectra as discussed below. Thus one finds the e_g band 4-6 eV above E_F, the $j_{eff} = \frac{1}{2}$ band ~ 1 eV above E_F, the empty and occupied parts of the $j_{eff} = \frac{3}{2}$ band just above and below E_F, respectively.

The occupied part of the O 2*p* PDOS can be measured by the fluorescence component of the O *K*-edge RIXS. We have taken spectrum k in Fig. 2d as the representative fluorescence spectrum. The E_F position for the fluorescence spectrum has been fixed under the assumption that $E_{em} = 528.2$ eV is the excitation threshold of the O *K*-edge XAS [photon energy c in Fig. 2a]. The combined occupied and unoccupied parts of the O 2*p* PDOS thus derived are plotted in Fig. 3a.

The obtained O 2*p* PDOS is compared with the DOS calculated by DFT (see Methods) in Fig. 3b. One can see good one-to-one correspondence between the experimental and calculated structures in the O 2*p* PDOS. In particular, the assumed non-bonding O 2*p*-band position well agrees with the peak position of the calculated non-bonding O 2*p* band. Nevertheless, the conclusion of the present paper will not be altered by the magnitude of the band gap unless it collapses and the system becomes metallic.

Low-energy multiplet and phonon satellites

In order to examine the effect of electron-phonon coupling and possible low-symmetry crystal field, an enlarged plot of the RIXS spectra in the low-energy region is shown in Fig. 4a. The "elastic" peak at $E_{loss} = 0$ eV is a superposition of the genuine elastic scattering (which should be very weak for the present π scattering geometry) and low-energy (0–20 meV) elastic and quasi-elastic scattering between the nearly degenerate five components of the $J_{eff} = 2$ ground state [see Fig. 1b]. The sharp peak at E_{loss} ~ 0.4 eV is due to excitation from the $J_{eff} = 2$ ground state to the $J_{eff} = 0$ and 1 excited states. The latter excitation is also observed by Raman scattering as described below. The weak peak at E_{loss} ~ 0.8 eV is an excited state of the t_{2g}^2 multiplet having the quantum number $J_{eff} = 2$ [Fig. 1b]. Unfortunately, the residual cubic splitting Δ_c of the $J_{eff} = 2$ state [Fig. 1b] is too small to be resolved in the RIXS spectra. Each of the quasi-elastic, E_{loss} ~ 0.4 eV, and ~ 0.8 eV peaks are accompanied by sub-peaks with ~ 80 meV intervals on the higher-energy side. These sub-peaks are attributed to phonon replicas, as described below.

Analyses using ligand-field multiplet theory

The magnitude of the SOC of the Os 5*d* states can be estimated from the O *K*-edge XAS [Fig. 2a]. X-ray absorption into the empty t_{2g} state observed at 528–530 eV is split into double peaks separated by $\frac{3}{2}\zeta$ ~ 0.7 eV. Note that for the effective angular momentum operator $\mathbf{l}_{eff}$, the SOC constant ζ', defined through the SOC energy $\zeta'\mathbf{l}_{eff} \cdot \mathbf{s}$, is given by $\zeta' \equiv -\zeta$ because $\mathbf{l}_{eff} \equiv -\mathbf{l}$ for the t_{2g} electrons[25], where $\mathbf{l}$ is the bare angular momentum operator. The cubic ligand-field (LF) splitting Δ_{LF} of the Os 5*d* level into t_{2g} and e_g [Fig. 1a] can also be estimated from the O *K*-edge XAS. From the broad absorption feature at 532–536 eV, the e_g component could be isolated by monitoring the RIXS intensity of the $J_{eff} = 2$ (t_{2g}^2) → $t_{2g}e_g$ energy-loss feature at E_{loss} ~ 5 eV [marked by a solid line in Fig. 2b] as a function of E_{in}: Thus obtained intensity plotted by the blue dashed curve at the bottom of Fig. 2a gives the e_g component, allowing us to obtain $\Delta_{LF} \simeq 4$ eV.

To interpret the RIXS spectra quantitatively, LF multiplet calculations were performed and their results are shown in Fig. 2e. (For details, see Methods.) The calculated d^2 multiplet (red curves) reproduces the observed loss peaks at E_{loss} ~ 0.4 and 0.8 eV (t_{2g}^2 part), and those at E_{loss} ~ 4 eV ($t_{2g}e_g$ part). The RIXS spectra in the blue shaded parts, $E_{loss} \simeq$ 2–4 and 6–7 eV, cannot be reproduced by the d^2 multiplet. We attribute these features to

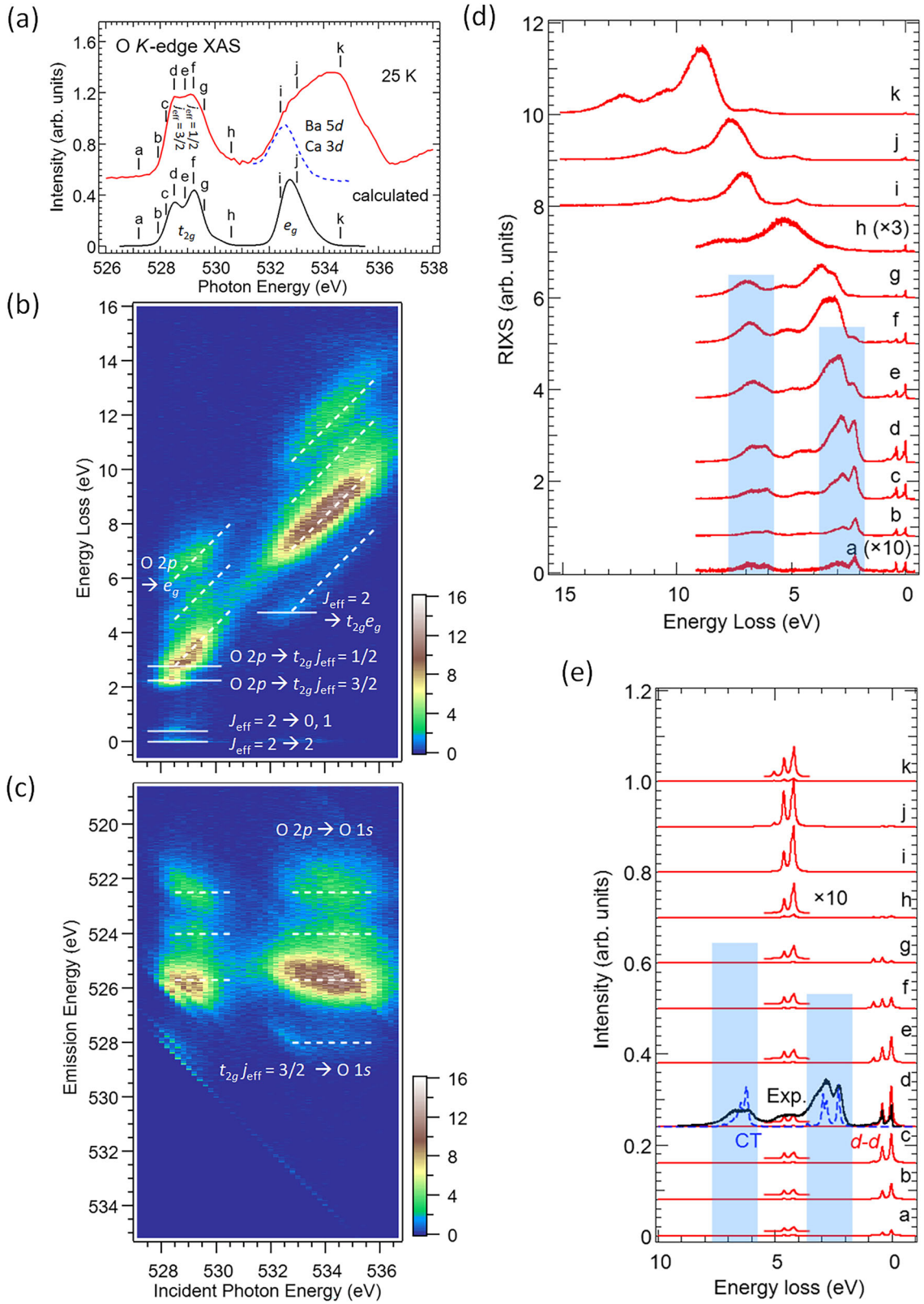

O 2p → empty Os 5d CT excitation, and simulate the CT excitation spectrum by $d^2 \rightarrow d^3$ multiplet calculation of inverse-photoemission leaving a hole in the non-bonding O 2p band. By assuming that the non-bonding O 2p band is located ~ 2 eV below E_F, as indicated by the DFT calculation, and by ignoring the p-band width, we could reproduce the CT spectrum from the $J_{eff} = 2$ ground state and plotted it by dashed blue curves in Fig. 2e. The $E_{loss} \simeq 2$–4 eV region arises from O 2p → t_{2g} excitation and the $E_{loss} \simeq 6$–7 eV region arises from O 2p → e_g CT excitation.

Note that there are no features in the RIXS spectra that indicate the lowering of the cubic symmetry: If the LF symmetry were lower than the cubic one, the $J_{eff} = 2$ ground state, which is split into the doublet E_g and the triplet T_{2g} [Fig. 1b], would be further split into multiple states as shown in

Fig. 2 | X-ray absorption spectroscopy (XAS) and resonant inelastic X-ray scattering (RIXS) spectra of Ba_2CaOsO_6 at the oxygen *K* edge recorded at 25 K. **a** XAS spectra. Top: XAS spectrum measured using the total fluorescence-yield method. The broad absorption band at 532–536 eV consists of transitions to the empty e_g states (blue dashed curve) as well as to the Ba 5*d*- and Ca 3*d*-derived conduction-band states. The blue dashed curve is the partial fluorescence-yield spectrum measured at E_{em} = 528 eV. Bottom: Spectrum calculated using ligand-field (LF) multiplet theory. See Methods. **b**, **c** Colored intensity maps of scattered X-rays: **b** as a function of incident X-ray energy E_{in} and energy loss E_{loss}. Solid lines mark the positions of constant E_{loss}. Dashed lines indicate those of constant E_{em}, **c** Scattered X-ray intensity map plotted against E_{in} and emission energy E_{em}. Dashed lines indicate constant E_{em}'s, corresponding to fluorescence from occupied states to the O 1*s* core level. **d** RIXS spectra measured for various E_{in}'s indicated by vertical bars at the top spectrum of (**a**). The shaded parts mark transitions from O 2*p* → Os 5*d* charge-transfer (CT) excitation. **e** LF multiplet calculation to simulate the RIXS spectra. The red curves show spectra arising from *d*-*d* excitation for a series of E_{in}'s indicated by vertical bars in the calculated O *K*-edge XAS spectrum shown at the bottom of (**a**). The dashed blue curves show O 2*p* → Os 5*d* CT excitation simulated by $5d^2 \rightarrow 5d^3$ multiplet calculation. The black curve is the measured RIXS spectrum for E_{in} = 528.5 eV [spectrum d in panel (**d**)].

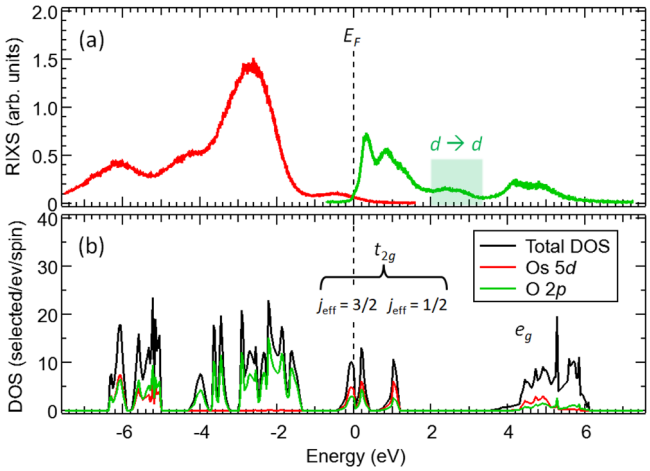

Fig. 3 | O 2*p* partial density of states (PDOS) derived from experiment and theory. **a** Experimental O 2*p* PDOS. The empty part is derived from the O 2*p* → Os 5*d* CT excitation in the RIXS spectrum [E_{in} = 528.2 eV, c in Fig. 2d], and the occupied part from the fluorescence component of the RIXS spectrum [E_{in} = 534.6 eV, k in Fig. 2d]. The shaded part marked by "$d \rightarrow d$" arises from $t_{2g}^2 \rightarrow t_{2g}e_g$ transition, and is unrelated to the O 2*p* PDOS. **b** PDOS of the nonmagnetic state obtained by the GGA+*U*+SOC calculation with $U - J_H$ = 2.5 eV.

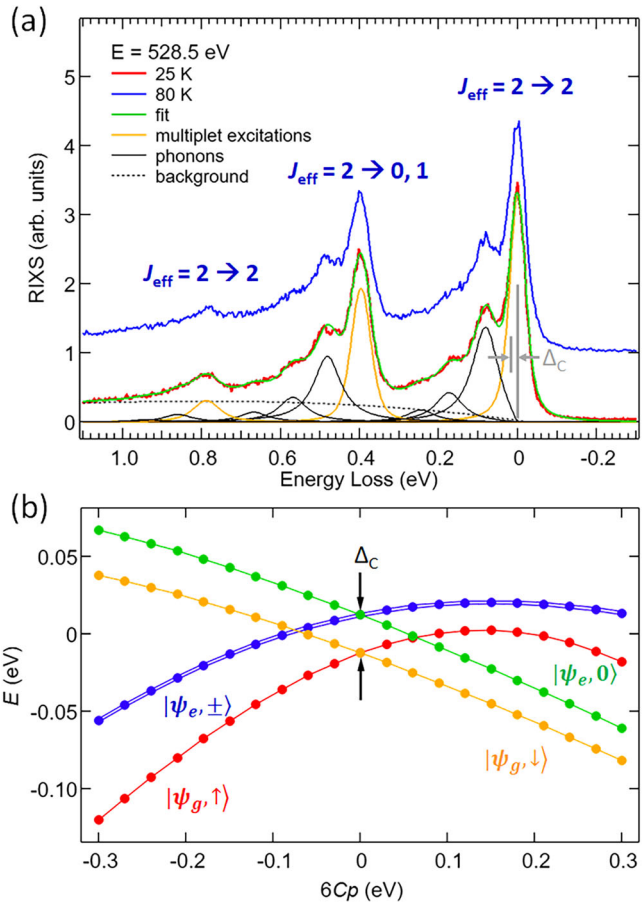

Fig. 4 | Low-energy excitations measured by O *K*-edge RIXS. Δ_c is the 'residual' cubic splitting of the J_{eff} = 2 ground state defined in Fig. 1b. **a** RIXS spectra in the low energy-loss region at different temperatures across the magnetic transition at $T^* \sim 50$ K for the incident photon energy of 528.5 eV. The *d*-*d* excitation shown in Fig. 1b is seen. The energy-loss peaks as well as the quasi-elastic peaks are accompanied by multiple phonon satellites. The splitting $\Delta_c \sim 20$ meV is not resolved in the spectra. Details of the line-shape analysis are given in Supplementary Note 1 with Supplementary Fig. 1 and Supplementary Table 1. **b** Energies of low-lying excited states of the Os^{6+} ($5d^2$) ion as functions of the low-symmetry D_{4h} LF parameter 6*Cp*[26], the splitting of the t_{2g} level. The O_h LF parameter Δ_{LF} is set to 4.1 eV. $|6Cp| \simeq 0.15$ reproduces the low-energy excitation in the O-*K* RIXS spectra of the $5d^1$ double perovskites[22,23].

Fig. 4b for cubic (O_h)-to-tetragonal (D_{4h}) symmetry lowering, and the low-energy part of the RIXS spectra would be significantly different from the experimental ones in Fig. 4a. If the tetragonal distortion were comparable to that of the $5d^1$ double perovskites Ba_2NaOsO_6[22] and Ba_2MgReO_6[23], which show peak at $E_{loss} \sim 0.1$ eV in the O *K*-edge RIXS spectra, the tetragonal crystal field 6*Cp*, which is equal to the tetragonal splitting of the t_{2g} level[26] should be as large as ± 0.15 eV, and the quasi-elastic $J_{eff} = 2 \rightarrow J_{eff} = 2$ peak would be split into a few peaks over an energy range of ~ 0.1 eV in addition to the phonon satellites. The absence of temperature dependence in the spectral line shapes across the magnetic transition at $T^* \sim 50$ K suggests that the magnetic transition does not involve any appreciable structural change. Furthermore, there are no spectral features that can be attributed to magnons nor bi-magnons, consistent with the absence of spin order in Ba_2CaOsO_6.

The octupolar nature of the ground state of the Os^{6+} ion in the O_h field can be demonstrated by LF multiplet calculation with a weak magnetic field in the (1,1,1) direction as a time-reversal symmetry-breaking perturbation that splits the non-Kramers E_g doublet into $|\psi_{g,+}\rangle$ and $|\psi_{g,-}\rangle$. For B = 10 T, we obtained octupolar moment $T_{xyz} \equiv \langle J^x J^y J^z \rangle \simeq 1.2$ with a tiny dipole magnetic moment of $\sim 8 \times 10^{-3} \mu_B$ induced along the (1,1,1) direction on top of the octupolar ground state. For a smaller field of B = 1 T, the induced dipolar moment was as small as $\sim 7 \times 10^{-4} \mu_B$. Generally, for a small field $B \ll \Delta_c/\mu_B$, the induced magnetic dipole moment along the direction of B ($\sim \mu_B B/\Delta_c$) is proportional to B. While ordering with the finite magnetic octupolar or electric quadrupolar moment can occur within the E_g ground state, the appearance of a finite magnetic dipolar moment requires hybridization between the E_g and T_{2g} states. Thus, to obtain a stable magnetic dipole order by the exchange interaction, a molecular field of $\mu_B B > \Delta_c$ at least is required.

Phonon Raman scattering

To further confirm the absence of low-symmetry crystal field, we employed Raman scattering spectroscopy, a sensitive probe of lattice symmetry. Figure 5a shows one-phonon Raman spectra of a Ba_2CaOsO_6 polycrystal taken at 80 K with two polarization geometries (∥ and ⊥; for technical details, see Methods). There must be phonons of $A_{1g} + E_g + T_{1g} + 2T_{2g} + 5T_{1u} + T_{2u}$ symmetries at the Brillouin-zone center in case of cubic $Fm\bar{3}m$ structure, out of which four (A_{1g}, E_g, and $2T_{2g}$) phonons are Raman-active.

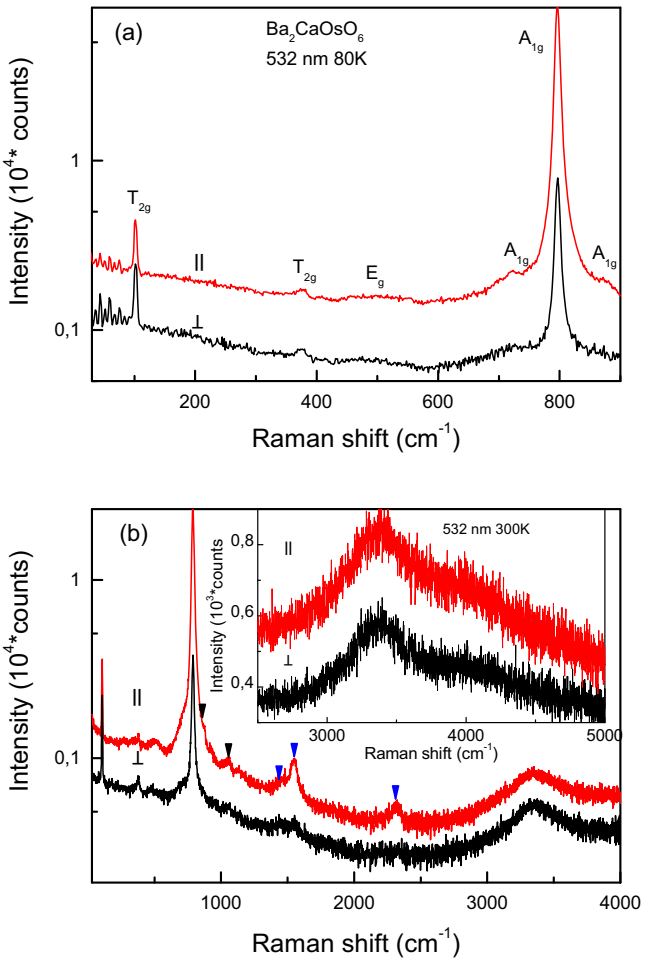

Fig. 5 | Raman spectra in two scattering symmetries. ∥ (red) and ⊥ (black) are presented. **a** Frequency range with one-phonon excitation. **b** Extended frequency range where the high-order phonon processes (blue arrows show features originating from the A_{1g} branch, black - another weak two-phonon features) and electronic excitation are seen. The latter seen in the range from 3000 to 5000 cm^{-1}, as shown in the inset, most probably due to the $J_{\text{eff}} = 2$ ground state to the $J_{\text{eff}} = 1, 0$ excited states seen by RIXS (Fig. 4).

To obtain information about the symmetry of the observed excitation, polarization measurements were performed in two geometries - with parallel (∥) and with mutually perpendicular (⊥) polarizations of the incident and scattered light. We utilized the rules that in isotropic or cubic systems the depolarization ratio $\rho = I_{\perp}/I_{\parallel}$ does not exceed 0.75 for totally symmetric modes, while it is close to 0.75 for non-totally symmetric ones[27]. One can see that the line at ~ 796.5 cm^{-1} obviously dominates in the ∥ spectrum and can be assigned to the A_{1g} mode, while the phonons at frequencies 102.5, 375, and 495 cm^{-1} are observed in both polarized ∥ and depolarized ⊥ spectra and are assigned to T_{2g}, T_{2g}, and E_g modes, respectively, with the help of the non-magnetic DFT calculation of phonon modes as described in Supplementary Note 2 with Supplementary Fig. 2. The broad peak at 720 cm^{-1} has a fairly low depolarization ratio (~0.2), which suggests its A_{1g} symmetry. While its origin is not clear, the symmetry lowering cannot split the A_{1g} mode without the increase of the unit cell. (Note also that the second intensive T_{2g} mode remains unsplit.) The appearance of this low intensity A_{1g} peak can be, e.g., due to imperfections of the crystal structure (e.g. there are indications of anti-phase boundary defects with disorder at the B sites and other types of defects[28–31]) or a two-phonon repetition of 375 cm^{-1} vibration. Thus, our Raman experiments do not detect any direct evidence of the symmetry lowering in the cubic Ba_2CaOsO_6.

To examine the possible lattice distortions across $T^* \sim 50$ K, we measured spectra at 10 K with better resolution and found only minor changes in the spectrum, such as further hardening and narrowing of the A_{1g} mode at ~ 796.5 cm^{-1}. Interestingly, the frequency and unique line width of the low-frequency T_{2g} mode did not change in the whole temperature range of 10–300 K.

The higher frequency range from 800 to 3000 cm^{-1} presented in Fig. 5b shows several peaks dominating in the ∥ geometry and hence of the A_{1g} symmetry. The weak peaks at 870 and 1055 cm^{-1} indicated by black arrows are probably two-phonon features. The peaks at 1450, 1540 and 2310 cm^{-1} shown by blue arrows can be associated with double and triple phonon scattering from the A_{1g} phonon branch. At higher frequencies (>3000 cm^{-1}), two broad peaks are observed. They are clearly seen in both polarization geometries (∥ and ⊥), as well as upon excitation by both used laser lines (532 and 633 nm, see Methods), which indicates Raman scattering by electron excitations of T_{2g} or E_g symmetry. Their energies agree well with the $J_{\text{eff}} = 2 \rightarrow J_{\text{eff}} = 0, 1$ RIXS peaks (Fig. 4).

Typically, in the case of $5d^2$ double perovskites, the effect of tetragonal distortions on the ground state is considered due to their stronger coupling with electronic structure[32]. Interestingly, Rayyan et al.[33] included the trigonal distortions in their analysis and demonstrated that, while these distortions are unable to split the E_g doublet due to symmetry constraints, they can lift the degeneracy of the higher-lying T_{2g} triplet. Under trigonal distortions, some of these T_{2g} states go to a lower energy. However, as shown in ref. 33 there is a rather wide range of trigonal distortion under which the non-Kramers E_g doublet remains the ground state. This doublet may, therefore, survive as the ground state under a small lattice distortion. It is also possible that distortion is substantially reduced due to dynamical Jahn-Teller effect. Whether the E_g doublet hosts an electric quadrupole or a magnetic octupole or both depends on the type of broken symmetry (spatial symmetry or time-reversal symmetry) and the strength of the mean field from neighboring Os ions.

Electron-phonon coupling effects on RIXS

In the low-energy RIXS spectra shown in Fig. 4, the quasi-elastic peak and the peak at $E_{\text{loss}} \simeq 0.4$ eV are accompanied by sub-peaks separated by ~80, 160, and 240 meV with decreasing intensities. We attribute the sub-peaks to phonon replicas created by the simultaneous excitation of optical phonons. The one-phonon energy of ~80 meV is somewhat lower but in a similar range as the Raman A_{1g} mode energies 720 cm^{-1} = 88 meV and 796.5 cm^{-1} = 99 meV. The replica energies are close to those observed in the RIXS spectra of Ba_2NaOsO_6[22]. From the replica intensities, the dimensionless electron-phonon coupling constant is estimated to be $M/\omega_0 \gtrsim 1$, where M is the average electron-phonon coupling matrix element and ω_0 is the phonon energy[34]. In spite of the moderately strong coupling, Jahn-Teller distortion is suppressed in Ba_2CaOsO_6 due to the strong SOC and dynamical Jahn-Teller effect, suggesting that Os-Os exchange interaction is strong enough to stabilize the magnetic octupole over the electric quadrupole. Here, it should be noted that sub-peaks similar to the phonon replicas may appear in the RIXS spectra if dynamical Jahn-Teller effect[35] exists, as reported for the $5d^1$ system Ba_2CaReO_6[18,19]. Whether such an effect also exists in $5d^2$ systems or not is an interesting question to be pursued in future studies. Considering the different time scales of RIXS (on the order of 0.01 fs) and Raman scattering (>10 fs), it is possible that dynamical Jahn-Teller effect was seen in RIXS as the "phonon replicas" but not in Raman scattering.

Discussion

We have investigated the electronic structure of Ba_2CaOsO_6 by XAS, RIXS, and Raman scattering experiment as well as DFT calculation, focusing on extracting reliable parameters characterizing the systems, as summarized in Table 1, and on the confirmation of the local cubic symmetry of the Os ions that favors the octupolar state as the origin of its 'hidden order'. We have also confirmed the octupolar nature of the non-Kramers E_g doublet ground state

Table 1 | Parameter values for the Os 5*d* electrons hybridized with O 2*p* orbitals in Ba_2CaOsO_6 derived in the present XAS and RIXS spectra

Parameter	Symbol	Value (eV)
ligand-field splitting	Δ_{LF}	4.1
Spin-orbit coupling for the 5*d* shell	ζ	0.47
Spin-orbit coupling for the t_{2g} shell	ζ'	−0.47
Hund's coupling for the t_{2g} shell	J_H	0.27

($|S_z| = 0$ and $|L_z| = 0$ under an infinitesimally small magnetic field) by LF multiplet calculation.

Owing to the hybridization between the O 2*p* and Os 5*d* orbitals, electronic excitation within the $5d^2$ multiplet and charge-transfer excitation from the occupied O 2*p* to the empty Os 5*d* states could be identified by the O *K*-edge RIXS. From comparison of the XAS and RIXS line shapes with the LF multiplet calculation, the absence of splitting of low-energy RIXS peaks as well as the lack of additional lines in Raman scattering spectra, we conclude that no crystal field lower than the cubic one can be identified, consistent with the small (~20 meV) residual cubic splitting of the $J_{eff} = 2$ ground state. The present results obtained by different types of X-ray and optical spectroscopy, which are typically very sensitive to a local environment of transition metals, substantially strengthen previous findings, in particular diffraction data demonstrating the absence of non-cubic distortions[14].

There are two possible mechanisms working hand-in-hand in suppressing the Jahn-Teller distortion expected for the Os^{6+} ion with the d^2 configuration. In both mechanisms, the strong SOC is involved. One is an on-site effect related to the stabilization of electrons not at cubic harmonics as the crystal field (i.e. Jahn-Teller effect) would prefer, but rather on entangled spin-orbitals[4,36]. Our RIXS measurements clearly resolved phonon replicas of the $J_{eff} = 2 \rightarrow 1, 0, 2$ excitation peaks. This allowed us to estimate the electron-phonon coupling strength, which turns out to be moderately strong, $M/\omega_0 \gtrsim 1$ and, therefore, may not be sufficiently strong to recover the Jahn-Teller distortion but might induce dynamical Jahn-Teller effect. On the other hand, there is also inter-site effect – the energy gain due to exchange interaction between the octupoles, which are formed by SOC. Further spectroscopic and theoretical studies are necessary to identify the octupolar order and its microscopic origin.

Methods

Materials preparation

Polycrystalline Ba_2CaOsO_6 was synthesized through a solid-state reaction using fine powders of BaO_2 (99% purity, Kojundo Chemical Laboratory Co., Ltd.), CaO_2 (prepared in the laboratory[37]), and Os (99.95% purity, Nanjing Dongrui Platinum Co. Ltd.) in a ratio of 2:1:1. Approximately 200 mg of the mixed materials were placed into an alumina crucible. The mixture was then heated in air to 1000 °C for 7 hours, followed by a 1-h dwell time, and subsequent cooling to room temperature over a span of 7 h. After re-mixing and pressing, the sample was annealed at 1000 °C for 24 h. The resulting product is a gray sintered pellet, possessing sufficient solidity to be manipulated with tweezers. Powder X-ray diffraction analysis was performed using Cu $K\alpha$ radiation within the $5° \le 2\theta \le 65°$ range at 293 K. The measurements were conducted with a MiniFlex600 diffractometer (Rigaku, Tokyo, Japan). The acquired data, shown in Supplementary Fig. 3, exhibited good agreement with simulations based on the crystallographic data of Ba_2CaOsO_6[12], confirming the single-phase nature of the product.

Resonant inelastic X-ray scattering

All resonant inelastic X-ray scattering (RIXS) and X-ray absorption spectroscopy (XAS) measurements at the O *K* edge were performed using the AGM-AGS spectrometer of beamline 41A at Taiwan Photon Source of National Synchrotron Radiation Research Center (NSRRC)[38]. This beamline is based on the energy compensation principle of grating dispersion[39]. The energy bandwidth of incident X-ray was 0.2 eV (0.1 eV for XAS measurement) while keeping the total energy resolution of RIXS as 30 meV at the incident photon energy of 528.5 eV. The sample surface was cleaned by scraping with a diamond file in the Ar glove box before the measurement and was transferred into the measurement chamber without exposure to the air. The base pressure of the measurement chamber was $\le 1 \times 10^{-8}$ Torr. The sample was cooled down to 25 K with liquid helium during the measurements. Both RIXS and XAS measurements were carried out using linear horizontally (π) polarized X-rays. The XAS spectra were measured with a normal-incident X-ray in the total fluorescence yield mode. For the RIXS measurement, the incidence angle was fixed at 20°, and the scattering angle was fixed at 90°. The combination of the π-polarized X-rays and the 90° scattering angle makes the RIXS signals purely magnetic. The same geometry also allowed us to reduce the elastic peak and to study low-energy excitation effectively.

Ligand-field multiplet calculation

Ligand-field multiplet (LF) calculations were performed by using the XTLS 8.5 package[40]. In the calculation of the O *K*-edge RIXS spectra, we assumed that the excited states of the $5d^2$ multiplet can be reached by O *K*-edge RIXS through the strong Os 5*d*-O 2*p* hybridization and could be simulated by the calculation of Os $L_{2,3}$-edge RIXS by setting the 2*p*-5*d* Slater integrals and the Os 2*p* core-level SOC to zero. While this simulation would give the energy positions of RIXS features correctly, it would not give correct intensities because relevant transition-matrix elements are not used. The O *K*-edge XAS [Fig. 2a] was also simulated by the Os $L_{2,3}$-edge XAS in the same manner.

In general, the Slater integrals *F*'s and *G*'s (anisotropy of Coulomb interaction) and the SOC coupling constant ζ in solids are smaller than those of isolated atoms, because the wavefunctions are more spatially extended due to hybridization. In order to model this effect, the atomic Slater integrals and ζ, deduced from Hartree-Fock calculations[41,42], were multiplied by constant factors R_{Slater} and R_{SOC} ($0 \le R_{Slater} < 1$, $0 \le R_{SOC} < 1$), respectively. These factors R_{Slater} and R_{SOC} and the cubic LF splitting Δ_{LF} were treated as adjustable parameters. For O *K*-edge RIXS, $\zeta = 0.50$ eV and $\Delta_{LF} = 4.1$ eV were used, and the Slater integrals between the Os 5*d* orbitals were reduced to 35% of the atomic Hartree–Fock values. Hund's coupling J_H between two *d* electrons (Table 1) is related to Slater integrals through $J_H = \frac{3}{49}F^2 + \frac{20}{441}F^4$[43]. The value $J_H = 0.27$ eV in the table is smaller than $J_H = 0.5$ eV used for the DFT+*U*+SOC calculation because the former is for the Os 5*d*-O 2*p* anti-bonding orbitals while the latter for the Os 5*d* atomic orbitals. The reduction of J_H from 0.5 eV to 0.27 eV suggests that the atomic orbitals consisting of the antibonding t_{2g} band have the weight Os 5*d*: O 2*p* ~70%: 30%.

In the calculation of the RIXS spectra, the same geometry as the experiment was adopted: The incident and scattered X-rays were set parallel to the cubic [001] and [100] directions, respectively. Taking the [001], [100], and [010] directions as the *z*, *x*, *y* axes, respectively, the linear polarizations of the incident and scattered X-rays were set to be (*x*, *y*) and (*x*, *z*), and the spectra for these two polarization sets were averaged.

The calculated spectra were broadened by a Voigt function, which is the convolution of a Lorentz function and a Gauss function. The widths (half width at half maximum, HWHM) of the Lorentz functions were determined from the natural lifetime of the core holes: 0.05 eV for the O *K*-edge RIXS[44]. The widths (standard deviation) of the Gauss functions were assumed to be 0.01 eV. The XAS and RIXS spectra were calculated for the five lowest states [the lowest $J_{eff} = 2$ state in Fig. 1b] as the initial state and were summed up according to the Boltzmann distribution of the initial states.

Raman spectroscopy

Raman measurements in the 10–300 K range were performed in back-scattering geometry from the polycrystalline sample using an RM1000 Renishaw microspectrometer equipped with a 532 nm solid-state laser and 633 helium-neon laser. Very low power (up to 1 mW) was used to avoid local heating of the sample. A pair of notch filters with a cut-off at 60 cm^{-1} were used to suppress light from the 633 nm laser line. To reach as close to

the zero frequency as possible, we used a set of three volume Bragg gratings (VBG) at 532 nm excitation to analyze the scattered light. The resolution of our Raman spectrometer was estimated to be 2–3 cm^{-1}.

The temperature dependence of the two narrow lines in the spectrum [Fig. 5a] turned out to be opposite. The fully symmetric line softened from 797.5 to 788.5 cm^{-1} with an increase in the temperature range from 10 to 300 K, and its width increased from 6.5 to 12 cm^{-1}, which can be explained by anharmonicity effects. In contrast to this behavior, the energy and width of the low-frequency T_{2g} phonon line remains constant within the measurement error ($\omega \sim 102.5\ cm^{-1}$ and $\Gamma \sim 1.5\ cm^{-1}$) when heated from 10 to 300 K. Unfortunately, the temperature behavior of the two broad lines - T_{2g} at 375 cm^{-1} ($\Gamma \sim 20\ cm^{-1}$) and E_g at 495 cm^{-1} ($\Gamma \sim 60\ cm^{-1}$) - is difficult to study due to their weak intensity. However, despite the large width of the lines, we did not find any signs of their splitting.

Density-functional-theory calculation

The generalized gradient approximation (GGA) in the form proposed by Perdew, Burke, and Ernzerhof[45] as realized in VASP code[46] was used for the density functional theory calculations. Phonon spectra shown in Supplementary Fig. 2 were calculated by the frozen phonon method[47] with $5 \times 5 \times 5$ mesh of the Brillouin zone of the $2 \times 2 \times 2$ supercell in non-magnetic GGA. Planewave cut-off was set up to 500 eV. The structure was relaxed until convergence in energy of 10^{-6} eV in electronic subsystem and 10^{-5} eV in ionic one was achieved.

Data availability

All data generated or analyzed during this study are available from the corresponding authors upon reasonable request.

Received: 30 November 2024; Accepted: 30 March 2025;
Published online: 27 April 2025

References

1. Takayama, T., Chaloupka, J., Smerald, A., Khaliullin, G. & Takagi, H. Spin–orbit-entangled electronic phases in 4*d* and 5*d* transition-metal compounds. *J. Phys. Soc. Jpn* **90**, 062001 (2021).
2. Khomskii, D. I. & Streltsov, S. V. Orbital effects in solids: Basics, recent progress, and opportunities. *Chem. Rev.* **121**, 2992 (2021).
3. Khomskii, D. I. & Streltsov, S. V. Magnetic oxides. In Chakraborty, T. (ed.) *Encyclopedia of Condensed Matter Physics*, 2nd ed., 98–111 (Academic Press, Oxford, 2024). https://www.sciencedirect.com/science/article/pii/B9780323908009001207.
4. Streltsov, S. V. & Khomskii, D. I. Jahn-Teller effect and spin-orbit coupling: Friends or foes? *Phys. Rev. X* **10**, 031043 (2020).
5. Chen, G. & Balents, L. Spin-orbit coupling in d^2 ordered double perovskites. *Phys. Rev. B* **84**, 094420 (2011).
6. Paramekanti, A., Maharaj, D. D. & Gaulin, B. D. Octupolar order in *d*-orbital Mott insulators. *Phys. Rev. B* **101**, 054439 (2020).
7. Svoboda, C., Zhang, W., Randeria, M. & Trivedi, N. Orbital order drives magnetic order in $5d^1$ and $5d^2$ double perovskite Mott insulators. *Phys. Rev. B* **104**, 024437 (2020).
8. Khaliullin, G., Churchill, D., Stavropoulos, P. P. & Kee, H.-Y. Exchange interactions, Jahn-Teller coupling, and multipole orders in pseudospin one-half $5d^2$ Mott insulators. *Phys. Rev. Res.* **3**, 033163 (2021).
9. Voleti, S., Pradhan, K., Bhattacharjee, S., Saha-Dasgupta, T. & Paramekanti, A. Probing octupolar hidden order via janus impurities. *npj Quantum Mater.* **8**, 42 (2023).
10. Hirai, D. et al. Detection of multipolar orders in the spin-orbit-coupled 5*d* Mott insulator Ba_2MgReO_6. *Phys. Rev. Res.* **2**, 022063(R) (2020).
11. Takahashi, A. & Shiba, H. Possible orbital orderings in a model of metallic double-exchange ferromagnets. *J. Phys. Soc. Jpn.* **69**, 3328 (2000).
12. Thompson, C. M. et al. Long-range magnetic order in the $5d^2$ double perovskite Ba_2CaOsO_6: comparison with spin-disordered Ba_2YReO_6. *J. Phys. Condens. Matter* **26**, 306003 (2014).
13. Cong, R. et al. Effects of charge doping on mott insulator with strong spin-orbit coupling, $Ba_2Na_{1-x}Ca_xOsO_6$. *Phy. Rev. Mater.* **7**, 084409 (2023).
14. Maharaj, D. D. et al. Octupolar versus Néel order in cubic $5d^2$ double perovskites. *Phys. Rev. Lett.* **124**, 087206 (2020).
15. Voleti, S., Maharaj, D. D., Gaulin, B. D., Luke, G. & Paramekanti, A. Multipolar magnetism in *d*-orbital systems: Crystal field levels, octupolar order, and orbital loop currents. *Phys. Rev. B* **101**, 155118 (2020).
16. Mazzone, D. G. et al. Antiferromagnetic excitonic insulator state in $Sr_3Ir_2O_7$. *Nat. Commun.* **13**, 913 (2022).
17. Lebert, B. W. et al. Nonlocal features of the spin-orbit exciton in Kitaev materials. *Phys. Rev. B* **108**, 155122 (2023).
18. Frontini, F. I. et al. Spin-orbit-lattice entangled state in A_2MgReO_6 (*A* = Ca, Sr, Ba) revealed by resonant inelastic X-ray scattering. *Phys. Rev. Lett.* **133**, 036501 (2024).
19. Iwahara, N. et al. Persistent quantum vibronic dynamics in a $5d^1$ double perovskite oxide. Preprint at https://arxiv.org/abs/2409.08095 (2024).
20. Lu, X. et al. Dispersive magnetic and electronic excitations in iridate perovskites probed by oxygen *K*-edge resonant inelastic x-ray scattering. *Phys. Rev. B* **97**, 041102(R) (2018).
21. Sala, M. M. et al. Orbital occupancies and the putative $j_{eff} = 1/2$ ground state in Ba_2IrO_4: A combined oxygen *K*-edge XAS and RIXS study. *Phys. Rev. B* **89**, 121101(R) (2014).
22. Agrestini, S. et al. Origin of magnetism in a supposedly nonmagnetic osmium oxide. *Phys. Rev. Lett.* **133**, 066501 (2024).
23. Živković, I. et al. Dynamic Jahn-Teller effect in the strong spin-orbit coupling regime. *Nat. Commun.* **15**, 8587 (2024).
24. Zimmermann, V. et al. Coherent propagation of spin-orbit excitons in a correlated metal. *npj Quantum Mater.* **8**, 53 (2023).
25. Kanamori, J. Theory of the magnetic properties of ferrous and cobaltous oxides I. *Prog. Theor. Phys.* **17**, 177 (1957).
26. van der Laan, G., Chopdekar, R., Suzuki, Y. & Arenholz, E. Strain-induced changes in the electronic structure of $MnCr_2O_4$ thin films probed by x-ray magnetic circular dichroism. *Phys. Rev. Lett.* **105**, 067405 (2010).
27. Strommen, D. P. Specific values of the depolarization ratio in Raman spectroscopy: Their origins and significance. *J. Chem. Educ.* **69**, 803 (1992).
28. Woodward, P., Hoffmann, R. & Sleight, A. Order-disorder in $A_2M^{3+}M^{5+}O_6$ perovskites. *J. Mater. Res.* **9**, 2118–2127 (1994).
29. Ting, V. et al. A structure and phase analysis investigation of the "1:1" ordered A_2InNbO_6 perovskites ($A = Ca^{2+}, Sr^{2+}, Ba^{2+}$). *J. Solid State Chem.* **179**, 551–562 (2006).
30. Bernuy-Lopez, C., Allix, M., Bridges, C. A., Claridge, J. B. & Rosseinsky, M. J. $Sr_2MgMoO_{6-\delta}$: structure, phase stability, and cation site order control of reduction. *Chem. Mat.* **19**, 1035–1043 (2007).
31. Vasala, S. & Karppinen, M. $A_2B'B''$ O_6 perovskites: A review. *Prog. Solid State Chem* **43**, 1 (2015).
32. Bersuker, I. B. *The Jahn-Teller Effect* (Cambridge University Press, Cambridge, 2006).
33. Rayyan, A., Liu, X. & Kee, H.-Y. Fate of multipolar physics in $5d^2$ double perovskites. *Phy. Rev. B* **108**, 045149 (2023).
34. Ament, L. J. P., van Veenendaal, M. & van den Brink, J. Determining the electron-phonon coupling strength from resonant inelastic X-ray scattering at transition metal *L*-edges. *Europhys. Lett.* **95**, 27008 (2011).
35. Iwahara, N. & Furukawa, W. Vibronic effect on resonant inelastic x-ray scattering in cubic iridium hexahalides. *Phys. Rev. B* **108**, 075136 (2023).
36. Streltsov, S. V., Temnikov, F. V., Kugel, K. I. & Khomskii, D. I. Interplay of the Jahn-Teller effect and spin-orbit coupling: The case of trigonal vibrations. *Phys. Rev. B* **105**, 205142 (2022).

37. Shi, Y. et al. Crystal growth and structure and magnetic properties of the 5*d* oxide Ca_3LiOsO_6: extended superexchange magnetic interaction in oxide. *J. Am. Chem. Soc.* **132**, 8474 (2010).
38. Singh, A. et al. Development of the Soft X-ray AGM-AGS RIXS beamline at the Taiwan Photon Source. *J. Synchrotron Rad.* **28**, 977 (2021).
39. Lai, C. H. et al. Highly efficient beamline and spectrometer for inelastic soft x-ray scattering at high resolution. *J. Synchrotron Rad.* **21**, 325–332 (2014).
40. Tanaka, A. & Jo, T. Resonant 3*d*, 3*p* and 3*s* photoemission in transition metal oxides predicted at 2*p* threshold. *J. Phys. Soc. Jpn.* **63**, 2788–2807 (1994).
41. Mann, J. B. Atomic structure calculations. i. hartree-fock energy results for the elements hydrogen to lawrencium. Tech. Rep., Los Alamos National Lab., Los Alamos, New Mexico https://www.osti.gov/biblio/4297173 (1967).
42. Herman, F. & Skillman, S. *Atomic Structure Calculations*, chap. 2, 1–17 (Prentice-Hall Inc., Englewood Cliffs, New Jersey, 1963).
43. Georges, A., de' Medici, L. & Mravlje, J. Strong correlations from Hund's coupling. *Annu. Rev. Condens. Matter Phys.* **4**, 137 (2013).
44. Krause, M. O. & Oliver, J. H. Natural widths of atomic *K* and *L* levels, *Kα* X-ray lines and several *KLL* Auger lines. *J. Phys. Chem. Ref. Data* **8**, 329–338 (1979).
45. Perdew, J. P., Burke, K. & Ernzerhof, M. Generalized gradient approximation made simple. *Phys. Rev. Lett.* **77**, 3865 (1996).
46. Kresse, G. & Furthmüller, J. Efficient iterative schemes for ab initio total-energy calculations using a plane-wave basis set. *Phys. Rev. B* **54**, 11169 (1996).
47. Togo, A. First-principles phonon calculations with phonopy and phono3py. *J. Phys. Soc. Jpn.* **92**, 012001 (2023).

Acknowledgements

We are grateful to M. Haverkort, A. Paramekanti, C. Franchini, and A. Hariki for useful discussions. The soft X-ray measurements were conducted at beam line 41A of Taiwan Photon Source. This work was partly supported by the National Science and Technology Council of Taiwan under Grant Nos. 103-2112-M-213-008-MY3, 108-2923-M-548 213-001, and 113-2112-M-007-033 and by the Japan Society for the Promotion of Science under Grant Nos. JP20K14416 and JP22K03535. We also thank the Ministry of Science and Higher Education of the Russian Federation for supporting Raman measurements and phonon calculations through funding the Institute of Metal Physics. Analysis of the results was supported by the Russian Science Foundation (Grant 23-42-00069). A.F. acknowledges the support from the Yushan Fellow Program and the Center for Quantum Science and Technology within the framework of the Higher Education Sprout Project under the Ministry of Education of Taiwan.

Author contributions

A.F., S.V.S. and D.J.H. coordinated the project. J.O., H.Y.H., A.S., D.J.H. and C.T.C. developed the RIXS instruments and conducted the RIXS experiments. Y.S.P. performed Raman experiments. H.H. and K.Y. synthesized and characterized the sample. G.S. and A.T. performed multiplet calculations. J.O., D.J.H., S.V.S. and A.F. analyzed the data and wrote the paper with inputs from other authors.

Competing interests

The authors declare no competing interests.

Additional information

Supplementary information The online version contains supplementary material available at https://doi.org/10.1038/s41535-025-00757-4.

Correspondence and requests for materials should be addressed to S. V. Streltsov, D. J. Huang or A. Fujimori.